

**Dieses Dokument ist eine Zweitveröffentlichung (Verlagsversion) /
This is a self-archiving document (published version):**

Quan Zhou, Zongbin Zhao, Zhiyu Wang, Yanfeng Dong, Xuzhen Wang, Yury Gogotsi, Jieshan Qiu

Low temperature plasma synthesis of mesoporous Fe₃O₄ nanorods grafted on reduced graphene oxide for high performance lithium storage

Erstveröffentlichung in / First published in:
Nanoscale. 2014, 6(4), S. 2286–2291 [Zugriff am: 04.11.2019]. Royal Society of Chemistry. ISSN 2040-3372.

DOI: <https://doi.org/10.1039/c3nr05423c>

Diese Version ist verfügbar / This version is available on:

<https://nbn-resolving.org/urn:nbn:de:bsz:14-qucosa2-362963>

„Dieser Beitrag ist mit Zustimmung des Rechteinhabers aufgrund einer (DFGgeförderten) Allianz- bzw. Nationallizenz frei zugänglich.“

This publication is openly accessible with the permission of the copyright owner. The permission is granted within a nationwide license, supported by the German Research Foundation (abbr. in German DFG).

www.nationallizenzen.de/

Low temperature plasma synthesis of mesoporous Fe₃O₄ nanorods grafted on reduced graphene oxide for high performance lithium storage†

Cite this: *Nanoscale*, 2014, 6, 2286Quan Zhou,^a Zongbin Zhao,^{*a} Zhiyu Wang,^b Yanfeng Dong,^a Xuzhen Wang,^a Yury Gogotsi^{ac} and Jieshan Qiu^{*a}

Transition metal oxide coupling with carbon is an effective method for improving electrical conductivity of battery electrodes and avoiding the degradation of their lithium storage capability due to large volume expansion/contraction and severe particle aggregation during the lithium insertion and desertion process. In our present work, we develop an effective approach to fabricate the nanocomposites of porous rod-shaped Fe₃O₄ anchored on reduced graphene oxide (Fe₃O₄/rGO) by controlling the *in situ* nucleation and growth of β-FeOOH onto the graphene oxide (β-FeOOH/GO) and followed by dielectric barrier discharge (DBD) hydrogen plasma treatment. Such well-designed hierarchical nanostructures are beneficial for maximum utilization of electrochemically active matter in lithium ion batteries and display superior Li uptake with high reversible capacity, good rate capability, and excellent stability, maintaining 890 mA h g⁻¹ capacity over 100 cycles at a current density of 500 mA g⁻¹.

Received 12th October 2013
Accepted 29th November 2013

DOI: 10.1039/c3nr05423c

www.rsc.org/nanoscale

Introduction

With a multi-billion dollar market value, rechargeable lithium-ion batteries (LIBs) have been the most popular power source for portable electronics due to their superior advantages, such as high energy density, long lifespan, no memory effect and environmental benignity.¹ They are also greatly desired for the continuously surging demand in large-scale energy applications, such as electric vehicles, renewable power plants and electric grids.^{2,3} This boosts a great deal of effort in the development of high-performance electrode materials that can store more energy efficiently. Fe₃O₄ is a very attractive anode material with high theoretical capacity (*ca.* 922 mA h g⁻¹), widespread availability, intrinsically enhanced safety, nontoxicity and low cost.^{4,5} More importantly, this inverse spinel possesses one of the highest electronic conductivities ($\sigma = 2 \times 10^4$ S m⁻¹) of the simple metal oxides, which makes it especially appealing as a high-power electrode material in LIBs, due to significantly

reduced electrode polarization.⁶ Despite the substantial merits, a major drawback of Fe₃O₄-based electrodes is the severe electrode pulverization caused by the drastic volume variation (up to 200%) during repeated electrochemical cycling and sluggish kinetics of conversion reaction.^{4,7} Macroscopically, this is manifested as poor cycling stability with low lithium storage capacities, especially at a high current rate. One way to improve the electrochemical performance of Fe₃O₄ is to use nanostructures with a short lithium diffusion path, large surface areas and enhanced reactivity, such as the nanoparticles, nanospheres, nanobelts and nanorods.^{8–16} Despite the observed high capacities of about 500–1000 mA h g⁻¹, lithium storage in most Fe₃O₄ based electrodes remains reversible only at slow rates of 0.1–1 C due to the insufficient structural stability.

A promising approach to further enhance the lithium storage capability of Fe₃O₄ based electrodes is to combine them with carbonaceous materials. The presence of elastic carbon not only serves as a physical buffering layer to cushion the mechanical stress associated with the volume change of Fe₃O₄ upon cycling, but also greatly improves the electronic conductivity of the electrode.^{4,17–24} In some cases, it can even construct a three-dimensional network to facilitate the charge transfer and reinforce the entire electrodes.^{25–28} So far, various Fe₃O₄/C composites, including carbon coated nanospindles/nanospheres/nanoparticles, Fe₃O₄/CNT composites, graphene-wrapped particles, carbon-coated Fe₃O₄/graphene hybrids, and 3D hierarchical Fe₃O₄/graphene composites, have been explored as high-performance electrodes in LIBs.^{4,11,17–32} Nevertheless, the fabrication of truly durable Fe₃O₄ based electrodes with

^aCarbon Research Laboratory, Liaoning Key Lab for Energy Materials and Chemical Engineering, State Key Lab of Fine Chemicals, School of Chemical Engineering, Dalian University of Technology, Dalian 116023, China. E-mail: zbzhaod@dlut.edu.cn; jqiu@dlut.edu.cn

^bPhysical Chemistry, Technical University of Dresden, Bergstraße 66b, 01062 Dresden, Germany

^cDepartment of Materials Science and Engineering, A. J. Drexel Nanotechnology Institute, Drexel University, Philadelphia, Pennsylvania 19104, USA

† Electronic supplementary information (ESI) available: Experimental section, TEM images of β-FeOOH/GO and Fe₃O₄/rGO, TGA curves of the Fe₃O₄/rGO, lithium storage performance and Nyquist plots of the electrodes. See DOI: 10.1039/c3nr05423c

satisfactory cyclability and high-rate performance still remains a significant challenge.

In this work, we report a simple approach for the synthesis of reduced graphene oxide (rGO) decorated with mesoporous Fe_3O_4 nanorods through one-pot reduction of the $\beta\text{-FeOOH}$ /graphene oxide (GO) composite in dielectric barrier discharge (DBD) H_2 plasma under ambient conditions. The method shows superior efficiency for the growth of graphene-based composites due to the low temperature and short time (typically 30 min). Characterization shows that mesoporous Fe_3O_4 nanorods are tightly combined with rGO in high mass loading (79 wt.%). When evaluated for lithium storage capability, the Fe_3O_4 /rGO composite exhibits a high capacity of *ca.* 890 mA h g^{-1} with exceptional capacity retention for 100 cycles at a current density of 500 mA g^{-1} . Even when cycled at very high current densities of 1000–3000 mA g^{-1} , it may still deliver high reversible capacities of 520–700 mA h g^{-1} due to the enhanced structural stability, electronic conductivity and kinetics for lithium storage.

Results and discussion

The synthetic strategy for the decoration of mesoporous Fe_3O_4 nanorods on rGO is illustrated in Scheme 1, and the synthesis experimental details are described in the ESI.† Firstly, $\beta\text{-FeOOH}$ nanorods are spontaneously grown on the surface of GO (denoted as $\beta\text{-FeOOH/GO}$) through the electrostatic adsorption and hydrolysis of Fe^{3+} on GO at 120 °C. Afterwards, $\beta\text{-FeOOH}$ nanorods are easily reduced to mesoporous Fe_3O_4 nanorods by active hydrogen species and high-energy electrons generated in the DBD hydrogen plasma. When bombarded by these energetic species, the polar chemical bonds in the oxygen-containing groups on GO are also distorted and ruptured. As a result, rGO is simultaneously formed to construct the composite with Fe_3O_4 .

The crystallographic structure and phase purity of the $\beta\text{-FeOOH/GO}$ sample were determined by X-ray powder diffraction (XRD), as shown in Fig. 1a. All the diffraction peaks can be assigned to tetragonal $\beta\text{-FeOOH}$ (JCPDS no. 34-1266).³³ No apparent signals from GO could be identified, indicating that $\beta\text{-FeOOH}$ particles are efficiently deposited on the surface of GO and suppress the stacking of GO layers.³⁴ The presence of

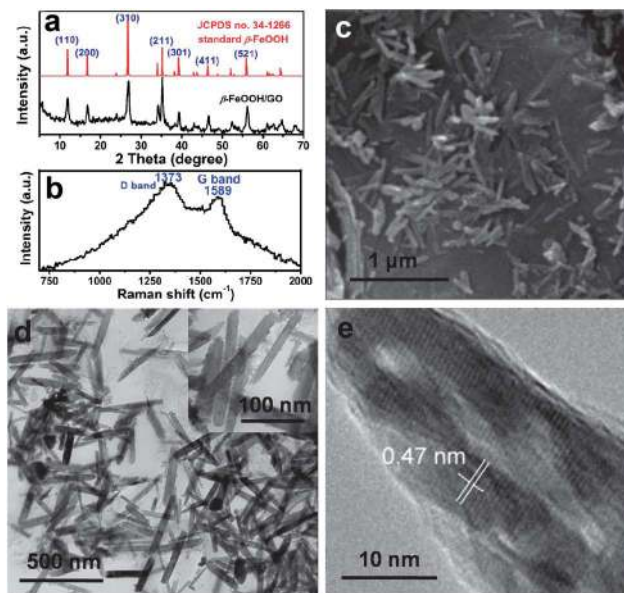
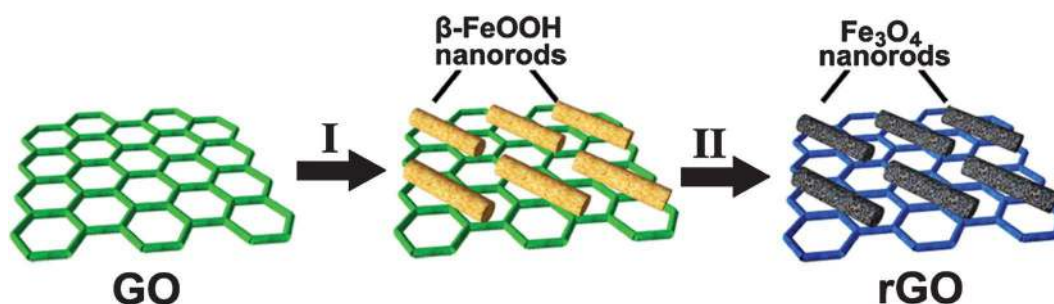


Fig. 1 (a) XRD patterns, (b) Raman spectrum, (c) SEM image and (d) TEM image of $\beta\text{-FeOOH/GO}$ sample, and (e) HRTEM image of a $\beta\text{-FeOOH}$ nanorod.

GO is evidenced by the Raman spectrum, as characterized by the D-band and G-band at Raman shifts of 1373 and 1589 cm^{-1} , respectively (Fig. 1b).³⁵ A panoramic view by using a scanning electron microscope (SEM) reveals a high density of $\beta\text{-FeOOH}$ nanorods on the surface of GO (Fig. 1c). Such a geometric confinement of metal oxide nanoparticles onto GO layers can enhance their interface contact and protect the particles from dissolution and agglomeration, thereby promoting the electrochemical activity and stability of the composite. Transmission electron microscopy (TEM) characterization further indicates the uniform distribution of $\beta\text{-FeOOH}$ nanorods on GO (Fig. 1d). These nanorods prepared in a higher initial concentration of FeCl_3 (e.g., 0.1 M), with the length of 300–400 nm and the diameter of 30–50 nm, are firmly anchored on GO even after drastic ultrasonication, showing the strong interaction between them. The high-resolution TEM (HRTEM) image validates the single-crystalline structure of $\beta\text{-FeOOH}$ nanorods. In Fig. 1e, the distinct lattice fringes with *ca.* 0.47 nm spacing correspond to



Scheme 1 Schematic illustration of rGO decoration with mesoporous Fe_3O_4 nanorods: (I) heterogeneous growth of $\beta\text{-FeOOH}$ nanorods on GO by forced hydrolysis of Fe^{3+} in aqueous solution; (II) one-pot reduction of GO supported $\beta\text{-FeOOH}$ nanorods to rGO decorated with mesoporous Fe_3O_4 nanorods by DBD hydrogen plasma.

the (210) planes of β -FeOOH. We suggest the preferential electrostatic attraction of Fe^{3+} to polar oxygen-containing groups on GO as the governing mechanism. The subsequent hydrolysis of Fe^{3+} and further ololation/oxolation of FeO_6 units may be responsible for the heterogeneous nucleation and growth of β -FeOOH nanoparticles on the GO surface.³⁶ In this process, a lower initial concentration of FeCl_3 (e.g., 0.015 M) results in the growth of sparse and smaller nanospindles on GO (Fig. S1†). Therefore, the size and growing density of β -FeOOH nanorods on GO can be readily tuned to achieve a desirable loading amount of active materials by simply varying the initial concentration of FeCl_3 in solution.

The β -FeOOH/GO composite possesses good structural stability and is robust enough to withstand hydrogen plasma. After the treatment, $\text{Fe}_3\text{O}_4/\text{rGO}$ can be derived from β -FeOOH/GO through the phase transformation of β -FeOOH to Fe_3O_4 (magnetite, JCPDS no. 19-0629) and simultaneous reduction of GO, as confirmed by XRD analysis (Fig. 2a). Due to the n-type doping effect on rGO (electron donating effect), the Raman spectrum of $\text{Fe}_3\text{O}_4/\text{rGO}$ shows a shift of the G-band to 1590 cm^{-1} (Fig. 2b). It suggests significant charge transfer and strong interactions between closely bonded rGO and Fe_3O_4 , which is beneficial to the electrochemical reactions.²⁸ The bands at 583 and 687 cm^{-1} can be ascribed to the T_{2g} and A_{1g} modes of Fe_3O_4 , respectively.³⁷ SEM and TEM examination shows that the conversion of β -FeOOH to Fe_3O_4 nanorods undergoes a topotactic transformation process due to their structural similarity, as shown in Fig. 2d–f. During the plasma treatment, high porosity is generated in the nanorods as a result of the volume contraction associated with the transformation

from low density β -FeOOH (3 g cm^{-3}) to denser Fe_3O_4 with a density of 5.17 g cm^{-3} . The N_2 adsorption/desorption isotherm of $\text{Fe}_3\text{O}_4/\text{rGO}$ shows a type IV curve with a type H3 hysteresis loop at relatively high pressure, corresponding to a specific surface area (calculated by the Brunauer–Emmett–Teller (BET) method) of ca. $86\text{ m}^2\text{ g}^{-1}$ and a mesopore size of $10\text{--}50\text{ nm}$ (Fig. 2c). Moreover, the TGA analysis indicates a high loading amount of 79 wt.% for Fe_3O_4 nanorods in this composite after subtracting the weight increase induced by the conversion of Fe_3O_4 to Fe_2O_3 , and the loading amount, the size and morphology of Fe_3O_4 can be easily tuned by controlling the initial ratio of GO and Fe source (Fig. S1 and S2†).

Fig. 3a shows representative discharge/charge voltage curves of the $\text{Fe}_3\text{O}_4/\text{rGO}$ composite at a moderate current density of 500 mA g^{-1} within a cut-off window of $0.01\text{--}3.0\text{ V}$. The initial discharge and charge capacities are found to be 1090 and 845 mA h g^{-1} based on total sample mass, respectively. The irreversible capacity loss of 22% may be mainly attributed to initial irreversible formation of Li_2O , and other irreversible processes such as trapping of some lithium in the lattice, formation of the solid-electrolyte interphase (SEI) and electrolyte decomposition, which are common for most anode materials, especially nanostructured ones.^{4,26} From the second cycle onwards, they exhibit a high discharge capacity of over 1000 mA h g^{-1} , which then stabilize at about 890 mA h g^{-1} after 100 cycles with a high coulombic efficiency of around 97–99% (Fig. S3†), corresponding to a capacity loss of 11%. This value is much higher than the theoretical capacity of graphite (372 mA h g^{-1}). Benefitting from its unique structure, the $\text{Fe}_3\text{O}_4/\text{rGO}$ composite also exhibits an excellent cycling response to a

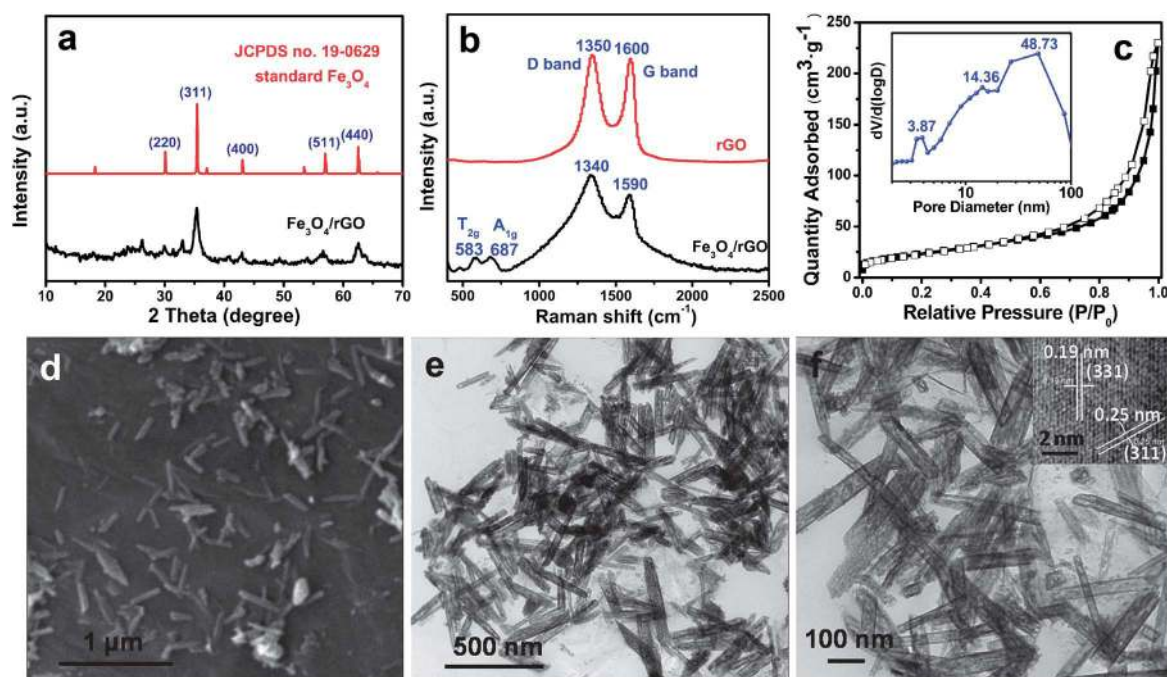


Fig. 2 (a and b) XRD patterns and Raman spectra of the $\text{Fe}_3\text{O}_4/\text{rGO}$ sample prepared in hydrogen plasma; (c) N_2 adsorption/desorption isotherm and corresponding pore size distribution of the $\text{Fe}_3\text{O}_4/\text{rGO}$ composite; (d) SEM image and (e and f) TEM images of rGO decorated with Fe_3O_4 nanorods. The inset in Fig. 2f is the HRTEM image of a Fe_3O_4 nanorod.

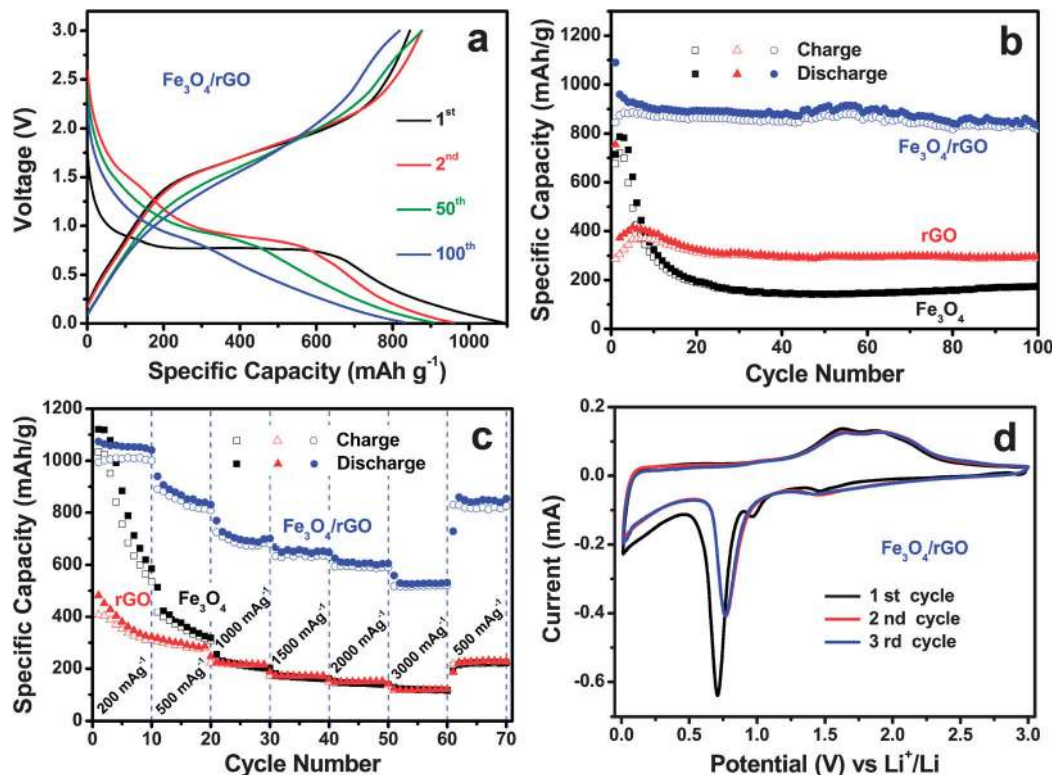


Fig. 3 (a) Discharge/charge voltage curves of the $\text{Fe}_3\text{O}_4/\text{rGO}$ composite; (b) comparative cycling performance of the $\text{Fe}_3\text{O}_4/\text{rGO}$ composite, pure Fe_3O_4 and rGO. For these tests, the data are taken at a current density of 500 mA g^{-1} within a voltage window of 0.01–3.0 V; (c) the rate capability of the $\text{Fe}_3\text{O}_4/\text{rGO}$ composite, pure Fe_3O_4 and rGO at different current densities; (d) cyclic voltammograms (CVs) of the $\text{Fe}_3\text{O}_4/\text{rGO}$ composite, obtained at a scan rate of 0.1 mV s^{-1} between 0.01 and 3.0 V.

continuously varying current rate. At a low current density of 200 mA g^{-1} , it delivers a higher capacity of *ca.* 1070 mA h g^{-1} than the theoretical value of pure Fe_3O_4 anode (922 mA h g^{-1}), probably due to surface lithium storage. Even when cycled at very high rates of $1000\text{--}3000 \text{ mA g}^{-1}$, high capacity of $700\text{--}520 \text{ mA h g}^{-1}$ still remains, as shown in Fig. 3c. Such a remarkable high-rate performance is superior to that of most Fe_3O_4 based electrodes,^{8–10,18–23,29,38} conventional electrodes, and other novel MXene materials as well.³⁹ After deep cycling at 3000 mA g^{-1} for ten cycles, a reversible capacity of *ca.* 800 mA h g^{-1} can be restored when cycling at a lower current density of 500 mA g^{-1} . To highlight the superiority of the $\text{Fe}_3\text{O}_4/\text{rGO}$ composite in lithium storage, the electrochemical performance of pure Fe_3O_4 and rGO prepared by the same method as $\text{Fe}_3\text{O}_4/\text{rGO}$ without introducing GO or FeCl_3 precursors is also investigated under the same conditions. The pure Fe_3O_4 particles deliver an initial discharge capacity of *ca.* 800 mA h g^{-1} but only *ca.* 25% of that can be retained after 20 cycles (Fig. 3b). Whereas for rGO, much lower capacities of $300\text{--}400 \text{ mA h g}^{-1}$ are delivered due to low theoretical capacity of carbonaceous materials. Under a high rate of $1000\text{--}3000 \text{ mA g}^{-1}$, both materials lose almost all of their capacities. Apparently, the tight integration of porous Fe_3O_4 nanorods and rGO significantly improves the electrochemical properties of their composite.

Moreover, spindle-like Fe_3O_4 (S- Fe_3O_4) can also be obtained by controlling Fe source concentration during the growth of $\beta\text{-FeOOH}$. The lithium storage performance of rGO decorated

with Fe_3O_4 nanorods (R- $\text{Fe}_3\text{O}_4/\text{rGO}$) and nanospindles (S- $\text{Fe}_3\text{O}_4/\text{rGO}$) was compared in Fig. S4.† Obviously, the cycling performance and specific capacity of S- $\text{Fe}_3\text{O}_4/\text{rGO}$ are remarkably lower than that of R- $\text{Fe}_3\text{O}_4/\text{rGO}$, which may be mainly attributed to the relatively poor structural stability of the spindle-like Fe_3O_4 and/or the improper ratio of Fe_3O_4 to rGO.

To uncover the electrochemical reaction involved in lithium storage in the $\text{Fe}_3\text{O}_4/\text{rGO}$ composite, cyclic voltammetry (CV) is performed within 0.01–3.0 V at a scan rate of 0.1 mV s^{-1} , as shown in Fig. 3d. In the first cycle, the cathodic peak centered at 1.47 V corresponds to the structure transition caused by lithium insertion into Fe_3O_4 ($\text{Fe}_3\text{O}_4 + x\text{Li}^+ + xe^- \rightarrow \text{Li}_x\text{Fe}_3\text{O}_4$). The intense peaks at *ca.* 0.71 and 0.96 V can be attributed to the reduction of $\text{Fe}^{3+}/\text{Fe}^{2+}$ to Fe^0 ($\text{Li}_x\text{Fe}_3\text{O}_4 + (8-x)\text{Li}^+ + (8-x)e^- \rightarrow 3\text{Fe} + 4\text{Li}_2\text{O}$), and the formation of amorphous Li_2O plus the irreversible reaction with the electrolyte. The broad anodic peak at 1.61–1.95 V corresponds to the restoration of Fe_3O_4 from Fe^0 . The subsequent curves show good reproducibility with a cathodic and anodic peak pair at *ca.* 0.8 V and 1.6–1.9 V for reversible conversion between Fe_3O_4 and Fe^0 , which is in good agreement with the literature report.^{10,25}

The excellent electrochemical performance of the $\text{Fe}_3\text{O}_4/\text{rGO}$ composite can be attributed to their rationally designed architecture. First, the highly elastic and stable rGOs not only serve as separators preventing the Fe_3O_4 nanostructures from aggregation, but also efficiently accommodate the volume change of Fe_3O_4 nanorods during electrochemical cycling, which ensures

the sustained structural integrity of the electrode. Second, the highly conductive rGO network provides an efficient pathway for fast charge transfer. In favor of the presence of rGO, the Fe₃O₄/rGO composite exhibits much lower resistance than the bare Fe₃O₄ nanoparticles, as evidenced by the drastically reduced size of the semicircle at high-frequency regions in the electrochemical impedance spectroscopy (EIS) patterns (Fig. S5†).⁴⁰ Third, appropriate size and internal porosity of Fe₃O₄ nanorods make them highly accessible to Li⁺ in the electrolyte and afford them the maximum structural stability by buffering volume expansion and internal mechanical stress induced by lithiation/delithiation with hollow spaces.^{41,42} This approach has been successfully used to develop silicon-containing anodes.⁴³ Moreover, Fe₃O₄ has an inverse spinel structure where 1/3 of the iron ions occupy the tetrahedral sites (all Fe³⁺), and 2/3 of the iron ions occupy both octahedral and tetrahedral sites (one half is Fe²⁺ and the other half is Fe³⁺). The electron exchange between the Fe³⁺ and Fe²⁺ endows Fe₃O₄ with very high electronic conductivities ($\sigma = 2 \times 10^4 \text{ S m}^{-1}$) at room temperature.⁶ This feature further facilitates the high-rate performance of the Fe₃O₄/rGO composite. Apparently, the high structural stability, enhanced electronic conductivity and the fast kinetics of lithium storage reaction determine the excellent electrochemical performance of the Fe₃O₄/rGO composite.

Conclusions

In summary, a low temperature plasma approach has been developed for the synthesis of mesoporous Fe₃O₄ nanorods grafted on rGO. The method shows superior efficiency to conventional annealing approaches due to the low temperature and short time (typically 30 min) for the reaction. Characterization shows that mesoporous Fe₃O₄ nanorods are tightly bonded to rGO and a high mass loading can be achieved. This well-designed nanostructure exhibits a stable high capacity of 890 mA h g⁻¹ after 100 cycles at a current density of 500 mA g⁻¹. Remarkably, excellent rate capability is also achieved, delivering high capacities of 700–520 mA h g⁻¹ at high current densities of 1000–3000 mA g⁻¹, respectively, which shows a promise of this anode material for high-power LIBs. Additionally, the plasma method has been also proven highly efficient for the production of graphene-based composites.

Acknowledgements

This work was supported by the NSFC (no. 51072028, 21176043). Collaboration between Drexel University and Dalian University of Technology was supported by the Cheung Kong Scholarship. The authors are thankful to Yulia Buranova for assistance with HRTEM analysis and to Michael Naguib for helpful comments (both at Drexel University).

Notes and references

- 1 M. V. Reddy, G. V. Subba Rao and B. V. R. Chowdari, *Chem. Rev.*, 2013, **113**, 5364–5457.
- 2 M. Armand and J. M. Tarascon, *Nature*, 2008, **451**, 652–657.
- 3 P. G. Bruce, B. Scrosati and J. M. Tarascon, *Angew. Chem., Int. Ed.*, 2008, **47**, 2930–2946.
- 4 W. M. Zhang, X. L. Wu, J. S. Hu, Y. G. Guo and L. J. Wan, *Adv. Funct. Mater.*, 2008, **18**, 3941–3946.
- 5 L. Zhang, H. B. Wu and X. W. Lou, *Adv. Energy Mater.*, 2013, DOI: 10.1002/aenm.201300958.
- 6 P. L. Taberna, S. Mitra, P. Poizot, P. Simon and J. M. Tarascon, *Nat. Mater.*, 2006, **5**, 567–573.
- 7 X. J. Zhu, Y. W. Zhu, S. Murali, M. D. Stollers and R. S. Ruoff, *ACS Nano*, 2011, **5**, 3333–3338.
- 8 Z. M. Cui, L. Y. Hang, W. G. Song and Y. G. Guo, *Chem. Mater.*, 2009, **21**, 1162–1166.
- 9 Y. Shi, M. Shi, Y. Qiao, J. Tu and H. Chen, *Nanotechnology*, 2012, **23**, 395601.
- 10 Z. Xiao, Y. Xia, Z. Ren, Z. Liu, G. Xu, C. Chao, X. Li, G. Shen and G. Han, *J. Mater. Chem.*, 2012, **22**, 20566–20573.
- 11 L. L. Wang, J. W. Liang, Y. C. Zhu, T. Mei, X. Zhang, Q. Yang and Y. T. Qian, *Nanoscale*, 2013, **5**, 3627–3631.
- 12 M. Y. Son, Y. J. Hong, J.-K. Lee and Y. C. Kang, *Nanoscale*, 2013, **5**, 11592–11597.
- 13 H. B. Wu, J. S. Chen, H. H. Hng and X. W. Lou, *Nanoscale*, 2012, **4**, 2526–2542.
- 14 J. S. Chen, T. Zhu, X. H. Yang, H. G. Yang and X. W. Lou, *J. Am. Chem. Soc.*, 2010, **132**, 13162–13164.
- 15 Z. Y. Wang, D. Y. Luan, S. Madhavi, C. M. Li and X. W. Lou, *Chem. Commun.*, 2011, **47**, 8061–8063.
- 16 B. Wang, H. B. Wu, L. Zhang and X. W. Lou, *Angew. Chem., Int. Ed.*, 2013, **52**, 4165–4168.
- 17 C. He, S. Wu, N. Zhao, C. Shi, E. Liu and J. Li, *ACS Nano*, 2013, **7**, 4459–4469.
- 18 C.-T. Hsieh, J.-Y. Lin and C.-Y. Mo, *Electrochim. Acta*, 2011, **58**, 119–124.
- 19 L. Li, T. Wang, L. Zhang, Z. Su, C. Wang and R. Wang, *Chem.–Eur. J.*, 2012, **18**, 11417–11422.
- 20 X. Li, X. Huang, D. Liu, X. Wang, S. Song, L. Zhou and H. Zhang, *J. Phys. Chem. C*, 2011, **115**, 21567–21573.
- 21 R. Wang, C. Xu, J. Sun, L. Gao and C. Lin, *J. Mater. Chem. A*, 2013, **1**, 1794–1800.
- 22 Q. Zhang, Z. Shi, Y. Deng, J. Zheng, G. Liu and G. Chen, *J. Power Sources*, 2012, **197**, 305–309.
- 23 J. S. Chen, Y. Zhang and X. W. Lou, *ACS Appl. Mater. Interfaces*, 2011, **3**, 3276–3279.
- 24 E. Kang, Y. S. Jung, A. S. Cavanagh, G.-H. Kim, S. M. George, A. C. Dillon, J. K. Kim and J. Lee, *Adv. Funct. Mater.*, 2011, **21**, 2430–2438.
- 25 G. M. Zhou, D. W. Wang, F. Li, L. L. Zhang, N. Li, Z. S. Wu, L. Wen, G. Q. Lu and H. M. Cheng, *Chem. Mater.*, 2010, **22**, 5306–5313.
- 26 W. Wei, S. Yang, H. Zhou, I. Lieberwirth, X. Feng and K. Muellen, *Adv. Mater.*, 2013, **25**, 2909–2914.
- 27 B. Li, H. Cao, J. Shao and M. Qu, *Chem. Commun.*, 2011, **47**, 10374–10376.
- 28 C. M. Ban, Z. C. Wu, D. T. Gillaspie, L. Chen, Y. F. Yan, J. L. Blackburn and A. C. Dillon, *Adv. Mater.*, 2010, **22**, E145–E149.

- 29 L. Ji, Z. Tan, T. R. Kuykendall, S. Aloni, S. Xun, E. Lin, V. Battaglia and Y. Zhang, *Phys. Chem. Chem. Phys.*, 2011, **13**, 7139–7146.
- 30 J. Su, M. Cao, L. Ren and C. Hu, *J. Phys. Chem. C*, 2011, **115**, 14469–14477.
- 31 T. Zhu, J. S. Chen and X. W. Lou, *J. Phys. Chem. C*, 2011, **115**, 9814–9820.
- 32 C. Lei, F. Han, D. Li, W. C. Li, Q. Sun, X. Q. Zhang and A. H. Lu, *Nanoscale*, 2013, **5**, 1168–1175.
- 33 X. L. Mou, B. S. Zhang, Y. Li, L. D. Yao, X. J. Wei, D. S. Su and W. J. Shen, *Angew. Chem., Int. Ed.*, 2012, **51**, 2989–2993.
- 34 X. B. Fan, W. C. Peng, Y. Li, X. Y. Li, S. L. Wang, G. L. Zhang and F. B. Zhang, *Adv. Mater.*, 2008, **20**, 4490–4493.
- 35 A. C. Ferrari, J. C. Meyer, V. Scardaci, C. Casiraghi, M. Lazzeri, F. Mauri, S. Piscanec, D. Jiang, K. S. Novoselov, S. Roth and A. K. Geim, *Phys. Rev. Lett.*, 2006, **97**, 187401.
- 36 Z. Y. Wang, D. Y. Luan, S. Madhavi, Y. Hu and X. W. Lou, *Energy Environ. Sci.*, 2012, **5**, 5252–5256.
- 37 H. P. Cong, X. C. Ren, P. Wang and S. H. Yu, *ACS Nano*, 2012, **6**, 2693–2703.
- 38 J. Zhang, Y. Yao, T. Huang and A. Yu, *Electrochim. Acta*, 2012, **78**, 502–507.
- 39 M. Naguib, J. Come, B. Dyatkin, V. Presser, P. L. Taberna, P. Simon, M. W. Barsoum and Y. Gogotsi, *Electrochem. Commun.*, 2012, **16**, 61–64.
- 40 Z. J. Fan, J. Yan, T. Wei, G. Q. Ning, L. J. Zhi, J. C. Liu, D. X. Cao, G. L. Wang and F. Wei, *ACS Nano*, 2011, **5**, 2787–2794.
- 41 J. W. Deng, H. X. Ji, C. L. Yan, J. X. Zhang, W. P. Si, S. Baunack, S. Oswald, Y. F. Mei and O. G. Schmidt, *Angew. Chem., Int. Ed.*, 2013, **52**, 2326–2330.
- 42 K. Evanoff, J. Benson, M. Schauer, I. Kovalenko, D. Lashmore, W. J. Ready and G. Yushin, *ACS Nano*, 2012, **6**, 9837–9845.
- 43 M. H. Ryou, J. Kim, I. Lee, S. Kim, Y. K. Jeong, S. Hong, J. H. Ryu, T. S. Kim, J. K. Park, H. Lee and J. W. Choi, *Adv. Mater.*, 2013, **25**, 1571–1576.